Contents lists available at ScienceDirect

Applied Catalysis B: Environmental

MOF-derived C-doped ZnO prepared *via* a two-step calcination for efficient photocatalysis

Lun Pan[a], Tahir Muhammad[a,b], Lu Ma[a], Zhen-Feng Huang[a], Songbo Wang[a], Li Wang[a], Ji-Jun Zou[a,*], Xiangwen Zhang[a,*]

[a] Key Laboratory for Green Chemical Technology of Ministry of Education, School of Chemical Engineering and Technology, Tianjin University; Collaborative Innovative Center of Chemical Science and Engineering (Tianjin), Tianjin 300072, China
[b] Department of Physics, The University of Lahore, 53700, Pakistan

ARTICLE INFO

ABSTRACT

ZnO is an important semiconductor that has been widely applied in solar cell, photocatalysis, environmental remediation. Doping and morphology control are important approaches to improve its photocatalytic performance. Herein, a facile two-step calcination method was developed to fabricate carbon(C)-doped cubic ZnO with porous structure from zeolite imidazolate frameworks (ZIF-8). Compared with one-step pyrolysis, the approach of two-step calcination not only retains the cubic morphology with interconnected ZnO nanoparticles and porous structure but also introduces C doping in ZnO lattice effectively. This morphology has advantage in charge transfer, optical absorption and mass transfer during the photoreaction, and C doping results in high charge-separation efficiency. The sample C350-400 (C-doped ZnO, firstly calcined at 350 °C for 2 h from ZIF-8, then 400 °C for 1 h) shows the maximum photoactivity, which is *ca*. 3-fold and 4-fold higher than ZnO (C450) in photodegradation and PEC water splitting (under UV–vis irradiation), respectively. It is expected that the preparation of metal oxide from MOF is a very promising way to fabricate highly efficient photocatalyst.

© 2016 Elsevier B.V. All rights reserved.

1. Introduction

ZnO (space group = $P6_3mc$, $a = 0.32495$ nm, $c = 0.52069$ nm) is a technologically important II–VI semiconductor with a wide direct band gap of ~3.3 eV at room temperature and a large exciton binding energy of approximately 60 meV [1], and it has been widely used in solar cells, photocatalysis, environmental remediation, piezoelectric nanogenerators, owing to its high catalytic efficiency, low cost, environmental sustainability and piezoelectric properties [2–9]. Many methods have been developed and applied to fabricate ZnO nanoparticles, such as simple hydrolysis, chemical vapor deposition, solvothermal treatment, electrodeposition, etc [1,8–12]. Recently, metal-organic frameworks (MOFs) has been used as precursors to fabricate porous metal oxides. For example, spindle-like porous α-Fe₂O₃ and hollow CuO octahedra were prepared from MIL-88-Fe and Cu-based MOFs, respectively, and applied for high-rate lithium-ion batteries [13,14]. In contrast to other precursors, MOFs provide the versatile and abundant choices in designing and constructing the hierarchically nanostructures, a family of polyfunctional organic compounds with variety of topological architectures and morphologies [14,15].

Generally, charge transfer and charge-pairs separation are vital for the photocatalysis [16–20]. First, ZnO has high electron mobility of 115–155 cm^2 V^{-1} s^{-1} (only 10^{-5} cm^2 V^{-1} s^{-1} for the most used TiO$_2$) [21], suggesting ZnO particles or clusters may serve as the good electron trappers and transmission medium. Therefore, the linkage of ZnO particles is beneficial for the photoperformance, owing to the rapid charge transfer *via* the boundary [22–24]. Second, the direct band gap of ZnO results low efficiency of charge separation [25]. To solve this, nonmetal doping of ZnO is an effective method to inhibit the charge-pair recombination and to realize the visible-light response [26–29]. The calculation of effective masses showed that ZnO typically possesses light electrons and heavy holes (intrinsic character of *n*-type semiconductor), while N, C and S doping can generally render electrons lighter and holes heavier, resulting in slower recombination rate of photogenerated electron-hole pairs [27]. Importantly, C doping can separate charge pairs most efficiently compared with N and S doping, serving as a potentially promising pathway to increase the quantum efficiency of ZnO-based photocatalysts [27]. Therefore, the combination of
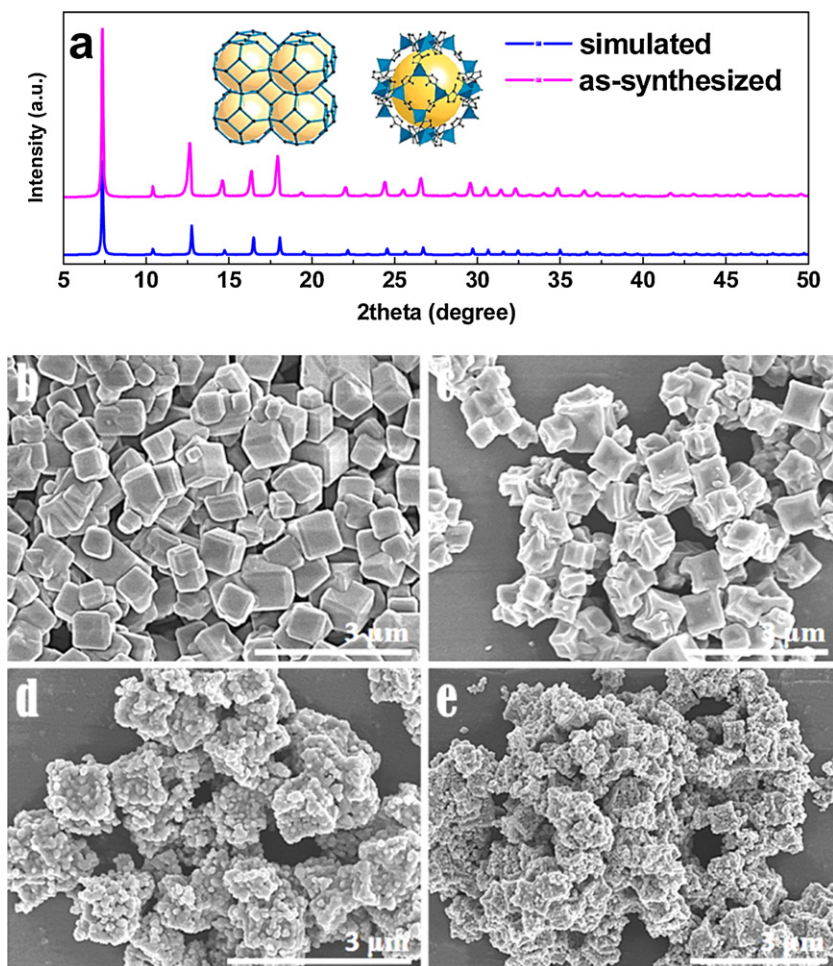
Fig. 1. XRD patterns (a) of synthesized ZIF-8 sample and the simulated pattern from crystal structure data, considering only framework atoms (i.e., contributions from solvent species within the cavities were excluded), and SEM images of ZIF-8 (b), C350 (c), C400 (d) and C450 (e). The inset in (a) is the stick diagram and largest cage in ZIF-8.

nanoparticle linkage and C doping is a promising approach to obtain the high photoactive ZnO.

There were a few methods developed for C doping in ZnO, like, self-doping *via* thermal pyrolysis of Zn containing inorganic-organic precursors [30,31], thermal plasma in-flight method [32], templated syntheses [33], solvothermal approach [26], and so on. But it is difficult to obtain C doping ZnO with porous structure (with connected ZnO nanoparticles) using these methods. Herein, we fabricated ZnO through two-step calcination method using zeolite imidazolate frameworks (ZIF-8) as the precursor. Importantly, the resulted sample simultaneously possesses original MOF morphology (porous structure with connected ZnO nanoparticles) along with abundant C doping. Therefore, the charge transfer and isolation are promoted (determined by EIS and PL spectra), accordingly, the photodegradation and photoelectrochemical (PEC) water splitting of the prepared samples are significantly increased.

2. Experimental

2.1. Materials

Rhodamine B (RhB), ethanol (chromatographic grade), 2-methyl-1H-Imidazole (reagent grade), ammonia solution (25 wt%), zinc acetate (reagent grade), phenol (reagent grade), and Na_2SO_4 (reagent grade) were purchased from Tianjin Guangfu Fine Chemical Research Institute. The commercial ZnO was purchased from

Aladdin (Shanghai). Deionized water (18.0 MΩ cm) was used in all experiments.

2.2. Sample preparation

0.878 g zinc acetate was first dissolved in 4.8 mL deionized water to form solution A, and 0.657 g 2-methyl-1H-Imidazole was dissolved in 8.704 g ammonia solution (25 wt%) to form solution B. Then, solution A was dropwised into solution B. The mixture was then vigorously stirred at room temperature for 4 h. The products were collected by centrifugation and washed with deionized water for several times. The samples were dried overnight at 60 °C in air. The resulted sample is ZIF-8.

Then, it was placed in the cable and calcined at 350 °C, 400 °C and 450 °C for 3 h at a heating rate of 5 °C/min, one-step resulting into samples of C350, C400 and C450, respectively. Besides, C350-400 and C350-450 were produced *via* two-step pyrolysis of ZIF-8 in the following progress: ZIF-8 was first calcined at 350 °C for 2 h at a heating rate of 5 °C/min, then the temperature was increased to 400 °C (or 450 °C) at a heating rate of 2 °C/min and maintained for 1 h.

2.3. Characterizations

XRD characterization was conducted using a D/MAX-2500 X-ray diffractometer equipped with Cu Kα radiation. SEM images were observed using a field-emission scanning electron micro-
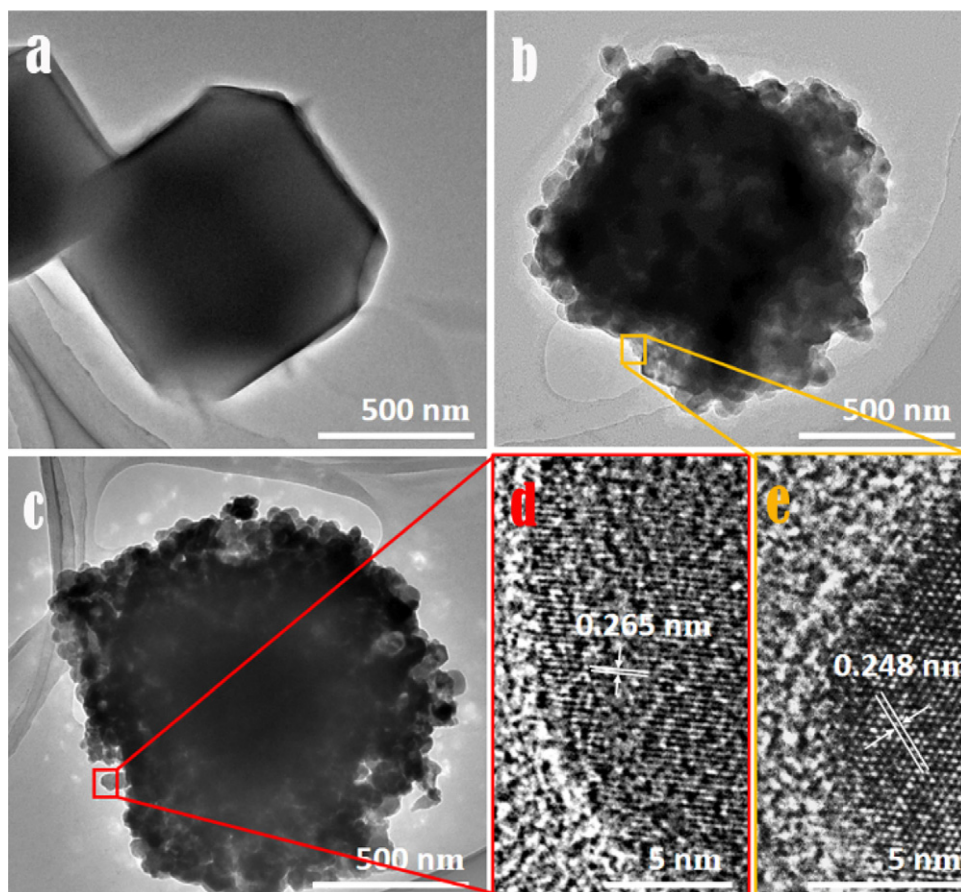
Fig. 2. TEM images of ZIF-8 (a), C400 (b,e) and C450 (c,d).

scope (Hitachi S-4800). High-resolution TEM observations were carried out with a Tecnai G^2 F-20 transmission electron microscope. Surface composition and chemical states were analyzed with a PHI-5000 X-ray photoelectron spectroscope (XPS) equipped with Al Kα radiation, and the binding energy was calibrated by the C1s peak (284.6 eV) of the contamination carbon. UV–vis diffuse reflectance spectra (UV-vis DRS) were recorded with a Hitachi U-3010 spectrometer equipped with a 60 mm diameter integrating sphere using BaSO$_4$ as the reflectance sample. Specific surface area (S_{BET}) and pore size distribution were calculated based on N$_2$ adsorption/desorption isotherms recorded on a Micromeritics Tri-Star 3000 instrument at 77 K, all calcined samples were outgassed under vacuum at 300 °C for 4 h. Steady-state photoluminescence (PL) spectra were measured by a Horiba JobinYvon Fluorolog3-21 with the excitation light at 325 nm.

2.4. Photocatalytic and photoelectrochemical (PEC) reactions

Photocatalytic degradation of organic dye was conducted in a closed quartz chamber (150 mL) vertically irradiated by a 300 W high-pressure xenon lamp (PLS-SXE300UV, Beijing Trusttech. Co., Ltd.) that located on the upper position. The irradiation area was *ca.* 20 cm^2. Reaction conditions: temperature, 25 ± 0.2 °C; C_0(RhB) = 20 μmol L^{-1} or C_0(phenol) = 400 μmol L^{-1}, catalysts: 0.2 g L^{-1}; no other reagents were added. Reaction was conducted by magnetic stirring under atmosphere, after stirring for 20 min in black to achieve adsorption equilibrium. Samples were withdrawn, centrifuged and analyzed using UV–vis spectrometer (U-3010, Hitachi Ltd.). The visible light (>420 nm) was obtained using the UV-cut optical filter (Beijing Trusttech. Co., Ltd.).
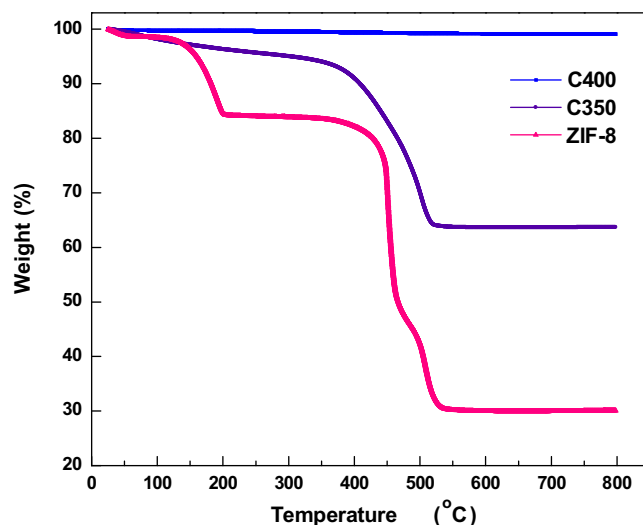

Fig. 3. TG curves of ZIF-8, C350 and C400.

PEC/Electrochemical properties were measured using an Ivium Vertex electrochemical workstation in a three-electrode cell with a Pt wire as the counter electrode and an Ag/AgCl reference electrode. Na$_2$SO$_4$ (0.2 M) was used as electrolyte solution. The working electrode was prepared by dip-coating ZnO slurry on an F-doped tin oxide (FTO) glass electrode (1 cm × 1 cm) and calcined at 200 °C for 1 h. Electrochemical impedance spectroscopy (EIS) measurements were carried out with a sinusoidal ac perturbation of 10 mV applied over the frequency range of 0.01–10^5 Hz.
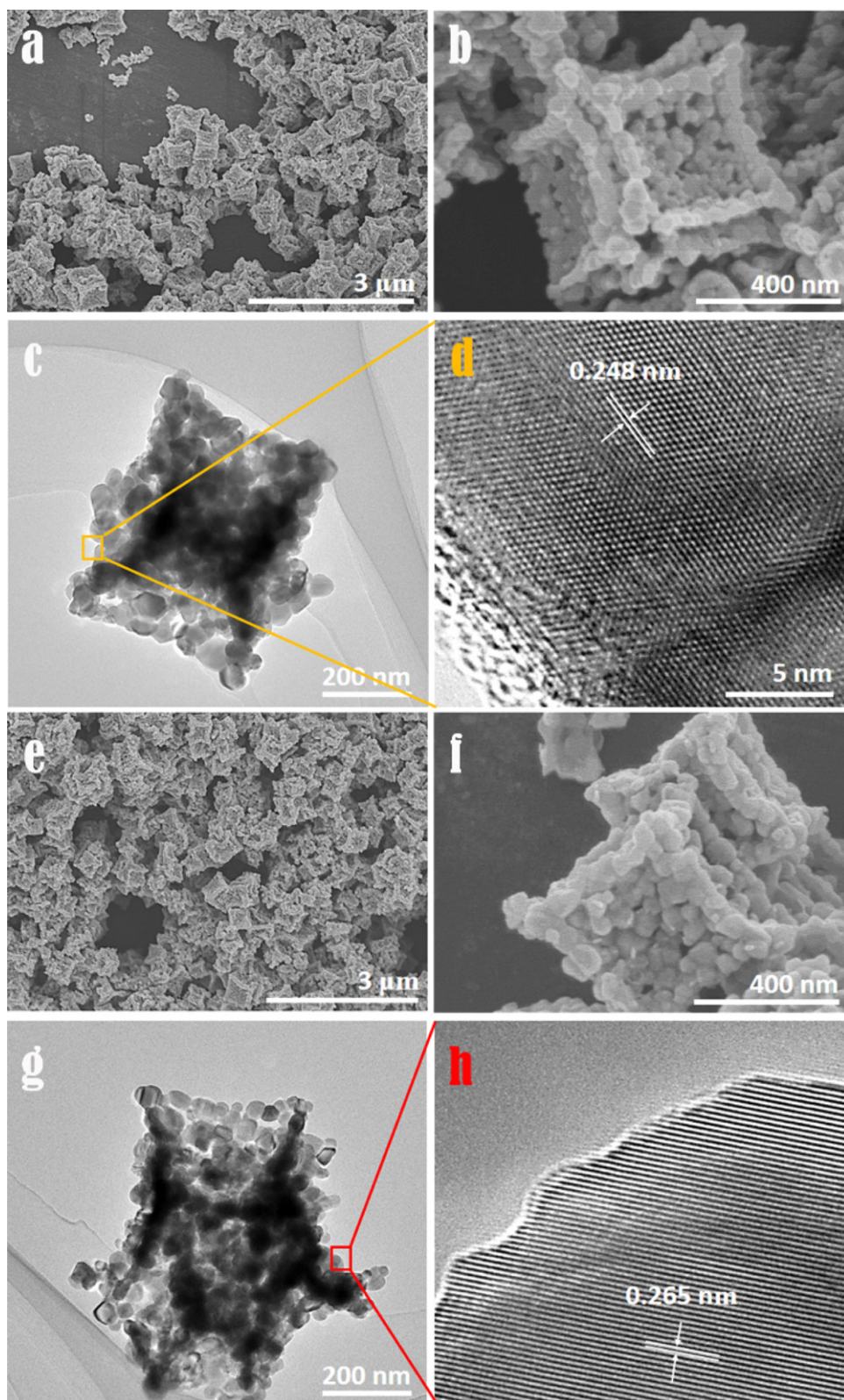
Fig. 4. SEM (a,b,e,f) and TEM (c,d,g,h) images of C350-400 (a–d) and C350-450 (e–h).

3. Results and discussion

3.1. Morphology and structure

XRD pattern of prepared ZIF-8 is shown in Fig. 1a, the sample shows the same characteristic peaks with the simulated ZIF-8.

From the experimental pattern of ZIF-8, a lattice constant of $a = 1.70174(5)$ nm was determined (cubic space group I-43 m), in agreement with the crystal structure [34,35]. ZIF-8 possesses large pores (11.6 Å) connected through small apertures (3.4 Å across) [34], and the framework of largest cage is connected by ZnN_4 tetra-

hedrons (the inset in Fig. 1a). SEM and TEM images in Fig. 1b and Fig. 2a show that ZIF-8 has uniform cubic shape, and the cubes with truncated edges expose six {1 0 0} faces and twelve {1 1 0} faces. The mean particle size is *ca.* 1 μm, similar to previous work[35]. With ZIF-8, the removal of organic groups by thermal calcination is expected to produce porous ZnO (with ZnO nanoparticles interconnected), similar to the hollow CuO derived from Cu-btc MOFs [13].

TG analysis of ZIF-8 (Fig. 3) was carried out, and there are two major weight losses: the weight loss at 190 °C is caused by the removal of residual water and unreacted 2-methylimidazole, and that at 450–510 °C is owing to the release of CO_2. It can be found that the direct calcination of ZIF-8 under the temperature above 500 °C can totally remove the organic groups to produce ZnO. However, high-temperature (>500 °C) calcination causes serious aggregation of ZnO particles (Fig. S1, Supplementary materials). Then, we conducted the calcination at relatively low temperature to prepare ZnO with retained morphology and porous structure for light absorption, electron transfer and mass transfer. From Fig. 3, the 400 °C calcination (for 3 h) is also able to produce pure ZnO, while only partial organic groups can be removed at 350 °C (for 3 h). Therefore, the applied calcination temperature should be in the range of 350–450 °C to produce ZnO from ZIF-8.

For C350, the morphology of ZIF-8 is maintained but with the {1 0 0} facet inner-shrinked (Fig. 1c). This is caused by the partial removal of organic groups (TG result). When the temperature is increased to 400 °C, C400 still shows the cubic morphology consisting of many ZnO nanoparticles (Fig. 1d). But TEM image (Fig. 2b) indicates ZnO aggregation happens. When the calcined temperature is further raised to 450 °C, C450 shows destroyed cubic shape and very serious aggregation of ZnO particles (Fig. 1e and Fig. 2c). For C400 and C450, ZnO particles are well crystallized with the crystal interplanar spacing of 0.248 nm and 0.265 nm (Fig. 2d,e).

The above indicates the low-temperature calcination is vital to produce the porous structure of ZnO (with ZnO nanoparticles interconnected), whereas high temperature is necessary to remove the organic groups but causes the structure collapse and serious aggregation of ZnO particles. Then how to control the calcined condition
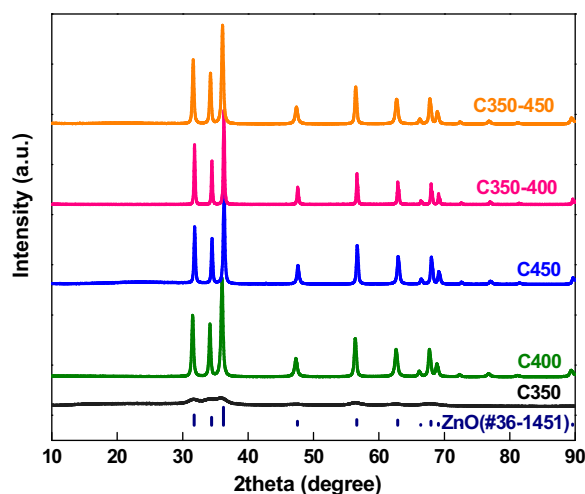

Fig. 5. XRD patterns of C350-450, C350-400, C450, C400 and C350.

to produce ZnO with both organic groups removed and porous structure?

Two-step calcination has been used to produce porous and uniform samples [36], the calcined temperature, time and heating rate can be tuned to modulate the size, morphology and crystallinity of materials. In this work, two-step calcination method was applied: ZIF-8 was first calcined under 350 °C for 2 h (at a heating rate of 5 °C/min) to partially remove the organic groups that result in the porous structure (see Fig. 1c), then the temperature was increased to 400 °C (or 450 °C) for 1 h (at a heating rate of 2 °C/min) to remove the residue organics and increase the crystallization of ZnO. As shown in Fig. 4, two-step calcination can make ZnO morphology stayed in cubic shape in the size of *ca.* 500–1000 nm. The resulted cubes are composed by many inter-connected ZnO nanoparticles, as detected in HR-TEM images with the crystal interplanar spacing of 0.248 nm and 0.265 nm (Fig. 4d,h). The XRD patterns (Fig. 5) show the samples with different calcined temperature all possess
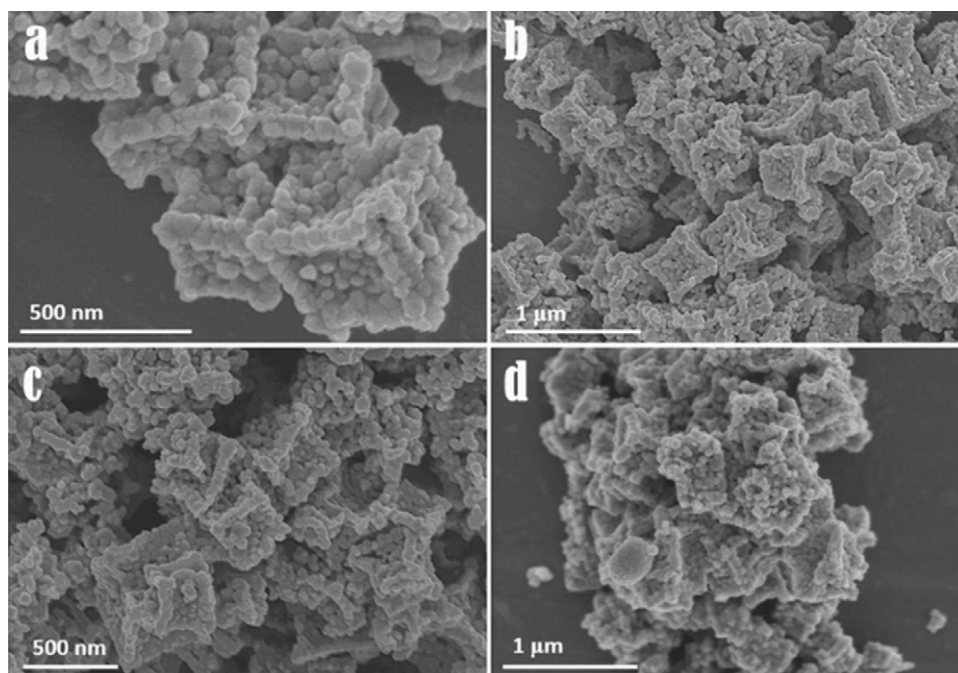

Fig. 6. SEM images of two-step calcined samples with different calcined time. (a) 350 °C for 1 h and 400 °C for 1 h; (b) 350 °C for 2 h and 400 °C for 2 h; (c) 350 °C for 2 h and 400 °C for 3 h; (d) 350 °C for 2 h and 400 °C for 4 h.
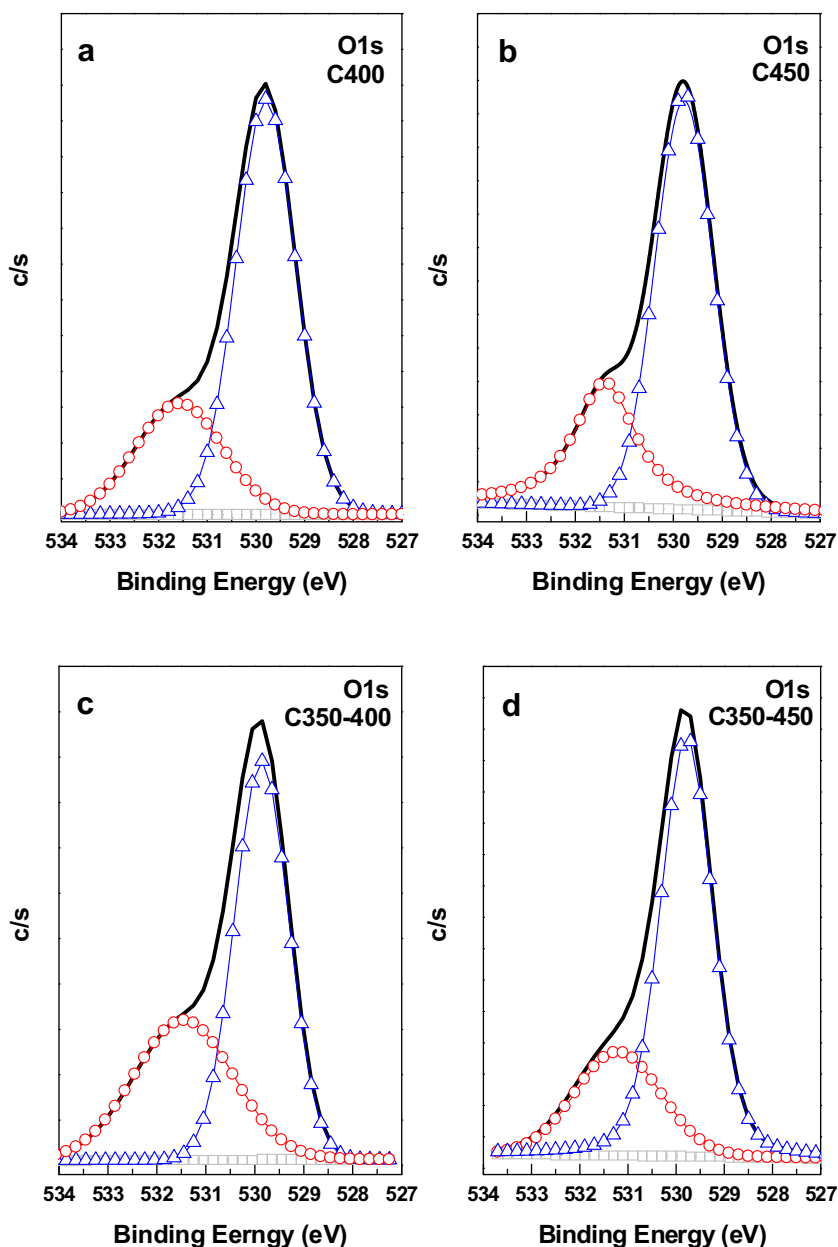
Fig. 7. XPS O1s of C400 (a), C450 (b), C350-400 (c) and C350-450 (d).

the typical wurtzite crystal. The peak intensity of C350 is very weak, because of the residual organic groups of ZIF-8 and low degree of ZnO crystallinity. The characteristic peaks become sharp and intense with high-temperature calcination (C400 and C450; C350-400 and C350-450), indicating the increase of ZnO particle size and crystallinity.

As shown in Fig. 6, the calcined time has influence on the structure of ZnO. Compared with C350-400 (calcined at 350 °C for 2 h and 400 °C for 1 h, Fig. 4a–d), the sample with shorter calcined time (Fig. 6a) has the same morphology but relatively lower crystallinity, while those with longer calcined time exhibit gradual aggregation (Fig. 6b–d). Therefore, the calcined time is very important to prevent the aggregation of ZnO particles and maintain the morphology with porous structure, and the optimized total time is 3 h.

Generally, polymer surfactants have often been used to control the porous structure of ZnO crystals [6]. In this work, direct calcination of ZIF-8 to remove its organic framework can release the volatile gases like CO_2 and H_2O, resulting in the porous structure of ZnO. But high temperature causes collapse of the framework, which

reduces the surface area (S_{BET}), e.g., S_{BET} for C400 and C450 are 13.65 and 0.60 m^2/g, respectively. The two-step method increases the surface area of ZnO. That is, C350-400 (17.82 m^2/g) and C350-450 (10.25 m^2/g) show higher surface area than C400 and C450, respectively. The isotherm curves of the samples are shown in Fig. S2 (Supplementary materials), the mesopores in C350-450 and C350-400 are 17 nm and 22 nm, respectively, while no pores are observed in C400 and C450. Therefore, the two-step calcined method benefits the formation of porous structure in ZnO. The above suggests the two-step calcination can introduce mesopores and inhibit the aggregation in ZnO. More importantly, the C doping can be introduced by this method, which will discussed in the following XPS spectra.

3.2. Surface chemical status and band structure

XPS characterization of prepared samples were conducted to investigate the chemical composition and status [37]. As shown in Fig. 7, O1s XPS of ZnO were fitted into two peaks centered at 531.5
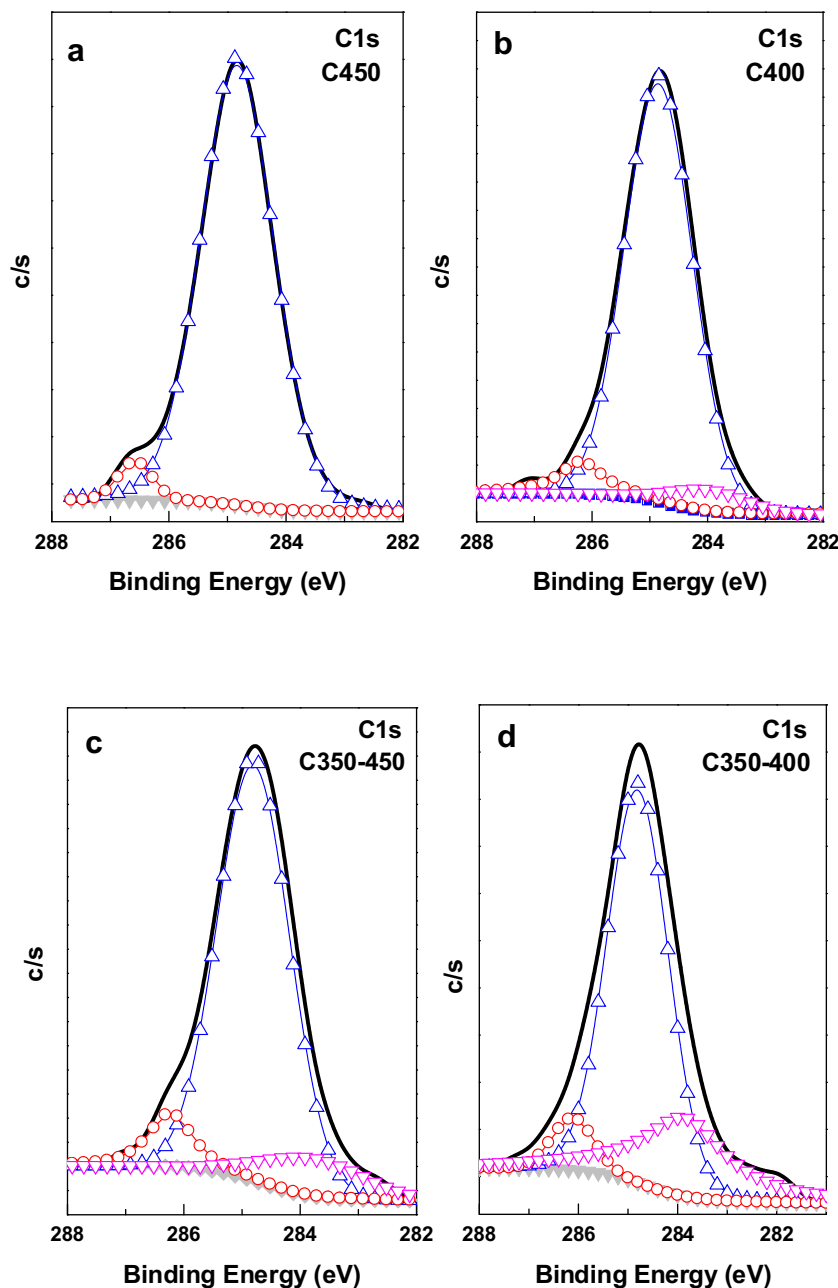
Fig. 8. XPS C1s spectra of C450 (a), C400 (b), C350-450 (c) and C350-400 (d).

and 529.8 eV. The high binding energy (BE = 531.5 eV) component is usually attributed to the chemisorbed or dissociated oxygen or OH species on ZnO, such as surface loosely bound oxygen species (OH group, H_2O or O_2) and carbonate species (i.e., $-CO_3$, C—O and C=O bonds)[38–40]. The peak on the low BE side of O1s spectrum at 529.8 eV is assigned to O^{2-} ions of Zn—O bonds in wurtzite structure with Zn^{2+} in hexagonal coordination [38]. Additionally, there are no obvious peaks of oxygen vacancies for the samples.

As shown in Fig. 8, four sets of peaks are observed in the C1s XPS spectra for C400, C450, C350-400 and C350-450, possessing a large peak with binding energy (BE) ranging from 282 to 288 eV. For C450 (Fig. 8a), the fitted major C1s XPS peak at about 284.6 eV is ascribed to adventitious hydrocarbon, while the small peak at 286.6 eV is surface loosely bound carbonate species (i.e., $-CO_3$, C—O and C=O bonds). When the calcined temperature was decreased to 400 °C (C400, Fig. 8b), a new fitted peak located at 283.8 eV appears, which

is due to Zn—C bonds caused by C doping [25]. When two-step thermal treatment was applied (C350-400 and C350-450, Fig. 8c,d), more dense peaks of Zn—C species are obtained, indicating two-step calcination can increase the C doping in ZnO crystal, among these samples, C350-400 possesses the highest C doped amount.

From Fig. 9a (Zn 2p spectra), the Zn $2p_{3/2}$ peak of C450 (pure ZnO) located at 1021.6 eV is symmetric, arised from Zn—O band[25]. It indicates the calcination under 450 °C can totally remove the organic groups of ZIF-8 without C doping. For C400, C350-450 and C350-400, a new peak located at *ca.* 1021.1 eV appears (Fig. 9b–d), which is referred to Zn—C bonds (C doping) [25]. It suggests that the low-temperature calcination and two-step calcination benefit the C doping in ZnO crystal, especially for the latter. Moreover, the C-doped amount for C400, C350-450 and C350-400 are about 1.9%, 3.6% and 5.4%, respectively. The results are consistent with C1s spectra, which suggests the effective C doping is dependent on
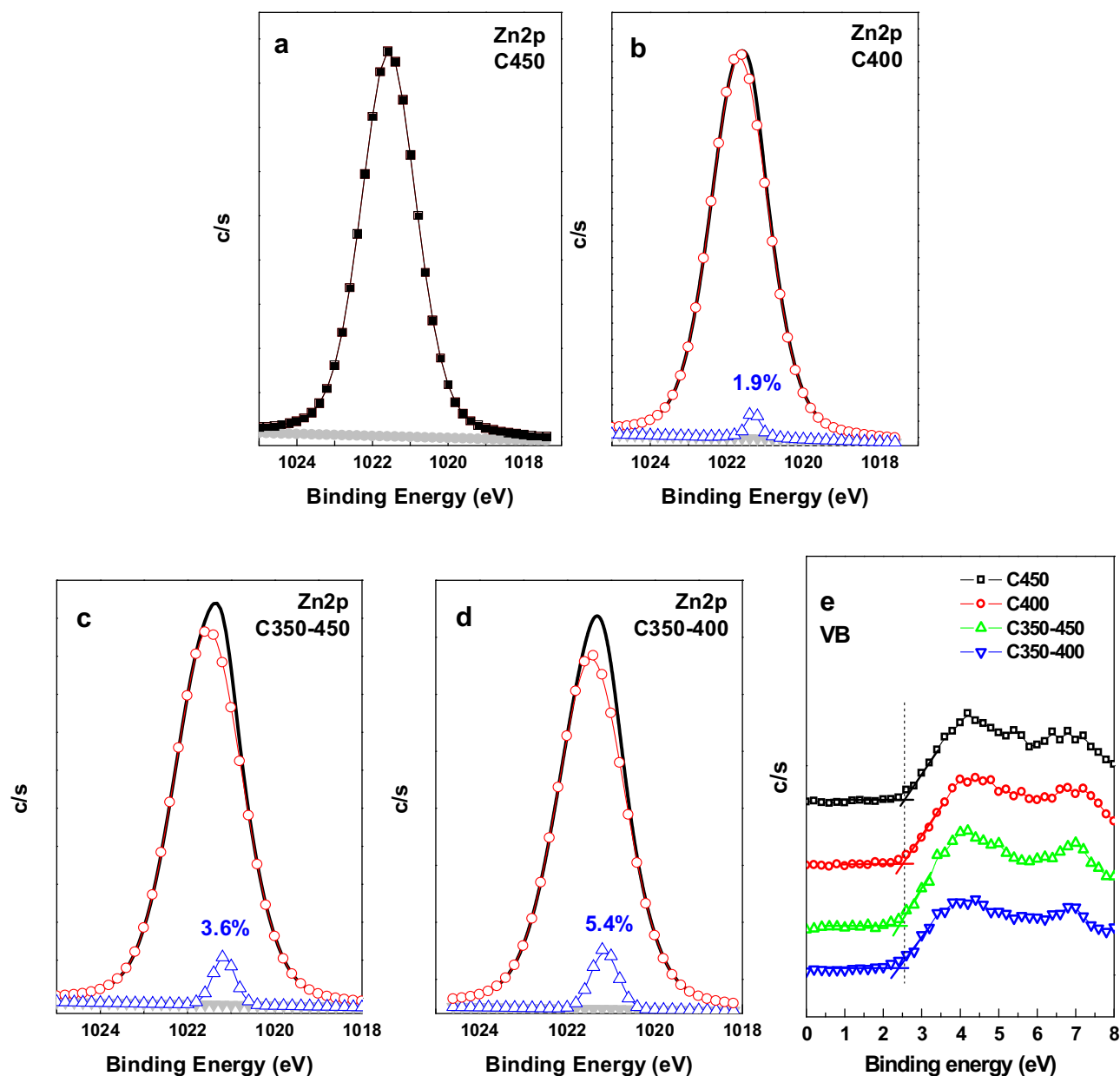
Fig. 9. Zn2p (a–d) and VB (e) spectra of C450, C400, C350-450 and C350-400.

the calcined temperature. High temperature can rapidly remove the C species to produce pure ZnO, while relatively low temperature provides the possibility of introducing carbon into the lattice of ZnO. Therefore, more C doping appears for C350-400 produced by mild calcination temperature.

Valence band (VB) XPS is a powerful tool to investigate the influence of impurity on the band structure of semiconductors [9,17,28,37]. VB spectra of prepared samples were conducted and shown in Fig. 9e. The valence band maximum (VBM) energy of C450 (pure ZnO) is approximately 2.53 eV relative to vacuum level, while C doping leads to the red shift of VBM, e.g., C400, 2.49 eV; C350-400, 2.43 eV; C350-450, 2.40 eV. This kind of red shift is resulted from the C doping [29,41], and the red-shift trend of VBM is the same with C-doping amount of prepared samples. Therefore, the two-step calcination is an effective approach to introduce C into the lattice of ZnO.

Furthermore, UV–vis DRS spectra were carried out and shown in Fig. 10a, in order to see the optical absorption of the samples. The

high optical absorption of C350 is caused by the partial existing of organic groups in ZnO. The thermally treated samples under higher temperature above 400 °C show the similar absorption spectra with pure ZnO (C450). However, there is slight red shift of absorption edge existing for C400, C350-450 and C350-400, owing to the narrowed band gap of ZnO that resulted from C doping [27]. Moreover, two-step calcined samples show higher optical absorption than the directly calcined samples, attributed to the regular cubic and porous structure of ZnO.

PL spectra of the prepared samples are shown in Fig. 10b. Since the majority of the optical absorption and subsequent photoexcitation take place within the surface region of photocatalyst, the emission is mainly due to the surface recombination [42]. Notably, the two-step calcined samples (C350-400 and C350-450) exhibit lower PL intensity than directly calcinced samples (C400 and C450), suggesting the former possesses higher efficiency in charge isolation. The result is consistent with the C doping amount in ZnO,
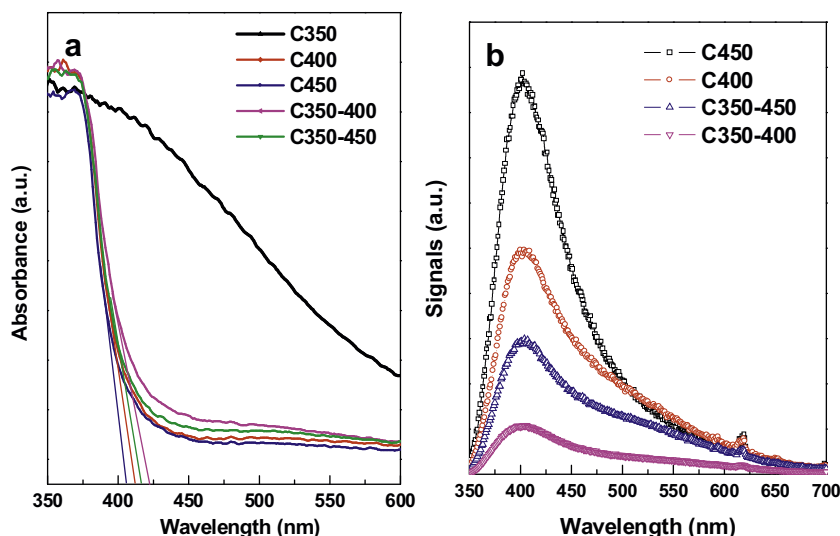
Fig. 10. UV–vis DRS pattern (a) and PL spectra (b) of C350, C400, C450, C350-400 and C350-450.

indicating the C doping is an effective approach to inhibit the charge recombination of electron-hole pairs.

3.3. Photocatalytic performance

The model photocatalytic reactions, degradation of organic dye (rhodamineB-RhB and phenol), were conducted to evaluate the photoactivity of the prepared samples. During the photodegradation, the formation of hydroxyl radical ($\bullet$OH) caused by electrons and holes is crucial[43–46]. Another important model is photo-electrochemical (PEC) water splitting, which is emerging as the promising methods for solar hydrogen and oxygen generation, and has attracted increasing interest [47–49]. In most case, the performance of PEC cell is largely determined by the properties of the electrode. With suitable band structure, ZnO is an excellent candidate to serve as the photoanode material [2]. Hence in this work, the above two typical photocatalytic tests were conducted to evaluate the photoactivity of ZnO.

The visible-light irradiation (>420 nm) was applied for the photodegradation of RhB and phenol (Fig. 11a,b). ZIF-8, C350, C450 and commercial ZnO show very low photoactivity as they cannot absorb visible light. For C-doped ZnO (C400, C350-400, C350-450 and 2.7%C-ZnO prepared according to Ref. [30]), the photoactivity is closely related to the C-doping amount. For example, C350-400 (5.4% C doping) shows *ca.* 1.2-fold, 1.7-fold and 1.8-fold higher photoactivity than C350-450 (3.6% C doping), 2.7%C-ZnO and C400 (1.9% C doping) in RhB degradation, respectively (Fig. 11a). In phenol photodegradation (Fig. 11b), C350-400 has *ca.* 1.3-fold, 2.4-fold and 2.9-fold higher photoactivity than C350-450, 2.7%C-ZnO and C400, respectively.

Fig. 11c,d shows the RhB and phenol photodegradation of prepared samples under UV–vis irradiation (Xenon light). The photoactivity trend is the same with that under UV–vis irradiation. ZIF-8 shows no photoactivity, and the activity of C350 is very low owing to large amount of organic residues and amorphous phase of ZnO. C400 and C450 exhibit moderate photoactivity. Importantly, two-step calcined samples (C350-400 and C350-450) show much higher photoactivity than the directly calcined samples. For example, C350-400 performs the highest photoactivity, more than 2-fold higher than those of directly calcined sample (C450 and C400), commercial ZnO and 2.7%C-ZnO. Additionally, C350-400 also shows high photostability (Fig. 11e), without no obvious deactivation after 5 degradation cycles.

The photodegradation results indicate the C doping is very important to enhance the photoactivity of C-doped ZnO, because it can inhibit the recombination of photoinduced charge pairs (Fig. 10b) and lead to the visible-light response [27]. Moreover, the photoactivity is also related to the surface area and porous structure. The higher surface area and porous structure benefit the adsorption of reactants on ZnO (Fig. S3, Supplementary materials), which facilitates reaction/interaction occurring on the surface or at the interface. Furthermore, the porous structure also enhances the optical absorption *via* light scattering [50].

Furthermore, the similar activity trend is observed in the photoelectrochemical (PEC) water splitting (Fig. 11f). Almost no photoactivity is observed for ZIF-8 and C350. C350-400 shows the highest PEC activity with the current density of 83 μA/cm^2 (at 1.23 V *vs* RHE), about 1.7-fold and 4-fold higher than that of C350-450 and C450 (or commercial ZnO, 2.7%C-ZnO), respectively.

Moreover, in electrochemical impedance spectroscopy (EIS), the arc radius of Nyquist plots can be used to evaluate the charge transfer resistance at the semiconductor/electrolyte interface, smaller arc radius implies smaller charge transfer resistance [51,52]. From Fig. 11g, it can be seen that two-step calcined samples (C350-400 and C350-450) show smaller radius than directly calcined samples (C350, C400 and C450), so charge in the former can be quickly transferred to reactant through the solid/liquid interface and consumed by chemical reaction, and the quick consumption of surface charges in turn retards the charge recombination or back charge transfer side processes. The high charge-separation efficiency of the two-step calcined sample is resulted from the C-doping and porous structure (with inter-connected ZnO nanoparticles). The results in EIS is well consistent with photocatalytic degradation and PEC performance.

Combining the above photoactivity and characterizations, it suggests that the photocatalytic activity of prepared ZnO is closely related to the charge-separation efficiency, which is attributed to C doping. Meanwhile, the porous structure with ZnO nanoparticle inter-connected also plays an important role, because it is beneficial for the mass transfer, charge transfer and light absorption during the photoreaction [53].

4. Conclusions

In this work, we have successfully synthesized C-doped cubic ZnO with porous structure by a facile two-step calcination of ZIF-8.
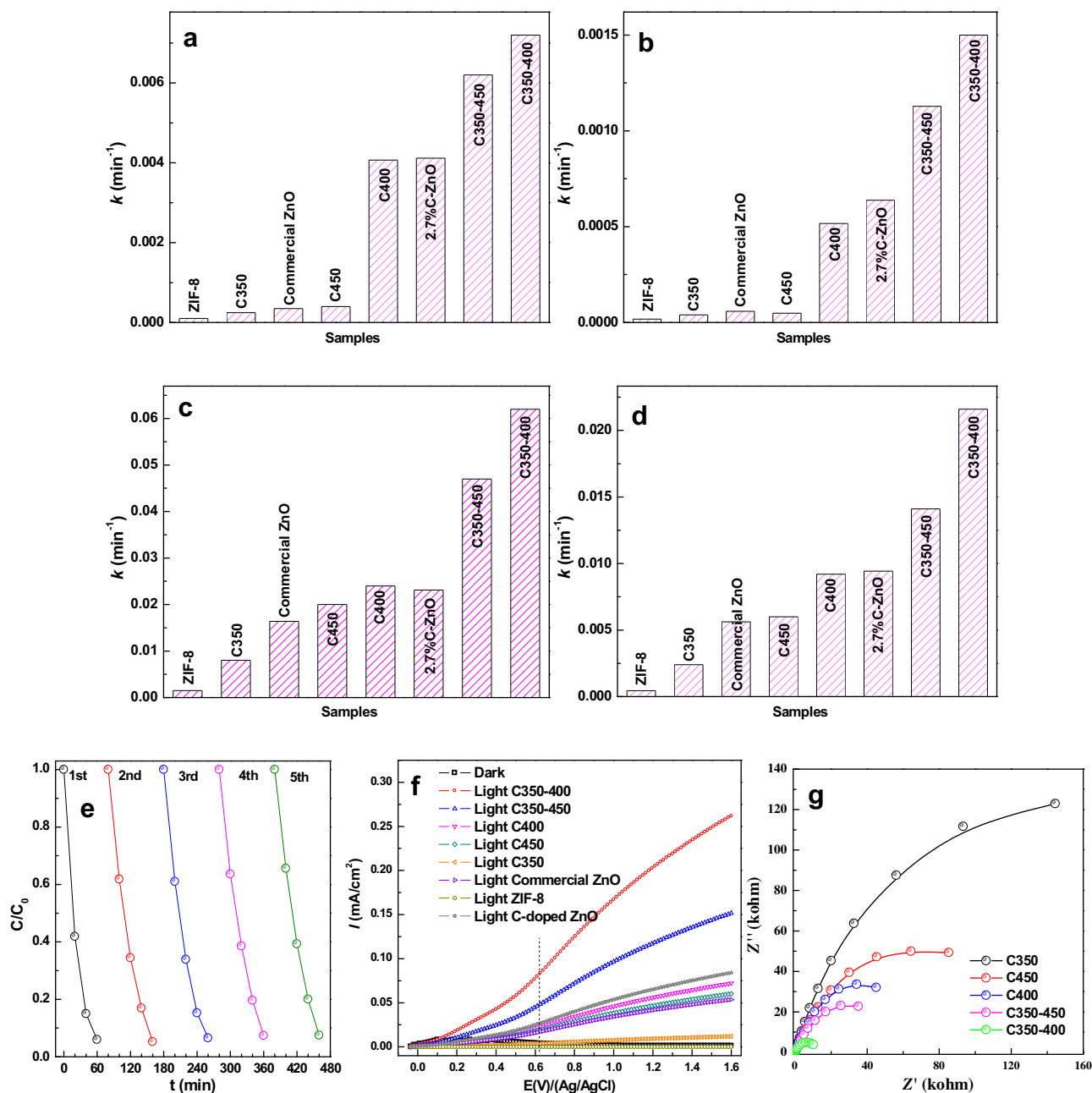
Fig. 11. The calculated reaction rates (k) for RhB (a) and phenol (b) photodegradation under visible light (>420 nm), k for RhB (c) and phenol (d) photodegradation under UV–vis light (Xenon light), the cycling of RhB photodegradation (UV–vis light) over C350-400 (e), current-voltage curve (f) and electrochemical impedance spectroscopy (EIS) of the prepared ZnO (g).

Compared with one-step calcination, this method has the merits of C doping in ZnO lattice and maintaining the porous cubic morphology, which benefits the electron-hole separation and optical absorption/mass transfer during the photoreaction. Therefore, two-step calcined sample (C350-400) shows *ca.* 3-fold and 4-fold higher photoactivity than pure ZnO (C450) in photodegradation and PEC applications (under UV–vis irradiation), respectively. It suggests that MOF may be a promising precursor to fabricate highly efficient photocatalyst.

Appendix A. Supplementary data

Supplementary data associated with this article can be found, in the online version, at http://dx.doi.org/10.1016/j.apcatb.2016.02.066.

References

[1] L. Schmidt-Mende, J.L. MacManus-Driscoll, Mater. Today 10 (2007) 40–48.
[2] S. Xu, Z.L. Wang, Nano Res. 4 (2011) 1013–1098.
[3] Z.L. Wang, J. Phys.: Condens. Matter 16 (2004) R829.
[4] Z.L. Wang, J. Song, Science 312 (2006) 242–246.
[5] D. Chen, Z. Wang, T. Ren, H. Ding, W. Yao, R. Zong, Y. Zhu, J. Phys. Chem. C 118 (2014) 15300–15307.
[6] Q. Zhang, C.S. Dandeneau, X. Zhou, G. Cao, Adv. Mater. 21 (2009) 4087–4108.
[7] S. Mukhopadhyay, P.P. Das, S. Maity, P. Ghosh, P.S. Devi, Appl. Catal. B: Environ. 165 (2015) 128–138.

[8] L. Pan, S. Wang, W. Mi, J. Song, J.-J. Zou, L. Wang, X. Zhang, Nano Energy 9 (2014) 71–79.
[9] L. Pan, G.-Q. Shen, J.-W. Zhang, X.-C. Wei, L. Wang, J.-J. Zou, X. Zhang, Ind. Eng. Chem. Res. 54 (2015) 7226–7232.
[10] C.-L. Hsu, S.-J. Chang, Small 10 (2014) 4562–4585.
[11] Y. Chen, H. Zhao, B. Liu, H. Yang, Appl. Catal. B: Environ. 163 (2015) 189–197.
[12] Ž. Petrović, M. Ristić, S. Musić, M. Fabián, J. Mol. Struct. 1090 (2015) 121–128.
[13] R. Wu, X. Qian, F. Yu, H. Liu, K. Zhou, J. Wei, Y. Huang, J. Mater. Chem. A 1 (2013) 11126–11129.
[14] X. Xu, R. Cao, S. Jeong, J. Cho, Nano Lett. 12 (2012) 4988–4991.
[15] Z.-F. Huang, J. Song, K. Li, M. Tahir, Y.-T. Wang, L. Pan, L. Wang, X. Zhang, J.-J. Zou, J. Am. Chem. Soc. 138 (2016) 1359–1365.
[16] G. Li, Z. Yi, H. Wang, C. Jia, W. Zhang, Appl. Catal. B: Environ. 158–159 (2014) 280–285.
[17] L. Pan, J.-J. Zou, S. Wang, Z.-F. Huang, A. Yu, L. Wang, X. Zhang, Chem. Commun. 49 (2013) 6593–6595.
[18] F. Kayaci, S. Vempati, C. Ozgit-Akgun, I. Donmez, N. Biyikli, T. Uyar, Nanoscale 6 (2014) 5735–5745.
[19] H. Yu, G. Cao, F. Chen, X. Wang, J. Yu, M. Lei, Appl. Catal. B: Environ. 160–161 (2014) 658–665.
[20] H. Yu, L. Xu, P. Wang, X. Wang, J. Yu, Appl. Catal. B: Environ. 144 (2014) 75–82.
[21] K. Park, Q. Zhang, B.B. Garcia, X. Zhou, Y.-H. Jeong, G. Cao, Adv. Mater. 22 (2010) 2329–2332.
[22] Q. Zhang, T.P. Chou, B. Russo, S.A. Jenekhe, G. Cao, Adv. Funct. Mater. 18 (2008) 1654–1660.
[23] Q. Zhang, T.P. Chou, B. Russo, S.A. Jenekhe, G. Cao, Angew. Chem. Int. Ed. 47 (2008) 2402–2406.
[24] T.P. Chou, Q. Zhang, G.E. Fryxell, G.Z. Cao, Adv. Mater. 19 (2007) 2588–2592.
[25] A.S. Alshammari, L. Chi, X. Chen, A. Bagabas, D. Kramer, A. Alromaeh, Z. Jiang, RSC Adv. 5 (2015) 27690–27698.
[26] M. Zhou, X. Gao, Y. Hu, J. Chen, X. Hu, Appl. Catal. B: Environ. 138–139 (2013) 1–8.
[27] W. Yu, J. Zhang, T. Peng, Appl. Catal. B: Environ. 181 (2016) 220–227.
[28] X. Chen, L. Liu, P.Y. Yu, S.S. Mao, Science 331 (2011) 746–750.
[29] X. Chen, C. Burda, J. Am. Chem. Soc. 130 (2008) 5018–5019.
[30] S. Cho, J.W. Jang, J.S. Lee, K.H. Lee, CrystEngComm 12 (2010) 3929–3935.
[31] H. Ouyang, J.F. Huang, C. Li, L. Cao, J. Fei, Mater. Lett. 111 (2013) 217–220.
[32] D.K. Mishra, J. Mohapatra, M.K. Sharma, R. Chattarjee, S.K. Singh, S. Varma, S.N. Behera, S.K. Nayak, P. Entel, J. Magn. Magn. Mater. 329 (2013) 146–152.
[33] Y.-G. Lin, Y.-K. Hsu, Y.-C. Chen, L.-C. Chen, S.-Y. Chen, K.-H. Chen, Nanoscale 4 (2012) 6515–6519.
[34] K.S. Park, Z. Ni, A.P. CoTé, J.Y. Choi, R. Huang, F.J. Uribe-Romo, H.K. Chae, M. O'Keeffe, O.M. Yaghi, Proc. Natl. Acad. Sci. U. S. A. 103 (2006) 10186–10191.
[35] M. He, J. Yao, Q. Liu, K. Wang, F. Chen, H. Wang, Microporous Mesoporous Mater. 184 (2014) 55–60.
[36] H.R. Radfarnia, M.C. Iliuta, Ind. Eng. Chem. Res. 52 (2013) 7002–7013.
[37] L. Pan, S. Wang, J.-J. Zou, Z.-F. Huang, L. Wang, X. Zhang, Chem. Commun. 50 (2014) 988–990.
[38] M. Chen, X. Wang, Y.H. Yu, Z.L. Pei, X.D. Bai, C. Sun, R.F. Huang, L.S. Wen, Appl. Surf. Sci. 158 (2000) 134–140.
[39] P.T. Hsieh, Y.C. Chen, K.S. Kao, C.M. Wang, Appl. Phys. A 90 (2008) 317–321.
[40] S. Major, S. Kumar, M. Bhatnagar, K.L. Chopra, Appl. Phys. Lett. 49 (1986) 394–396.
[41] L. Pan, J.-J. Zou, S. Wang, Z.-F. Huang, X. Zhang, L. Wang, Appl. Surf. Sci. 268 (2013) 252–258.
[42] A.B. Djurišić, W.C.H. Choy, V.A.L. Roy, Y.H. Leung, C.Y. Kwong, K.W. Cheah, T.K. Gundu Rao, W.K. Chan, H. Fei Lui, C. Surya, Adv. Funct. Mater. 14 (2004) 856–864.
[43] C. Chen, W. Ma, J. Zhao, Chem. Soc. Rev. 39 (2010) 4206–4219.
[44] L. Pan, J.-J. Zou, X. Zhang, L. Wang, J. Am. Chem. Soc. 133 (2011) 10000–10002.
[45] K. Rajeshwar, M.E. Osugi, W. Chanmanee, C.R. Chenthamarakshan, M.V.B. Zanoni, P. Kajitvichyanukul, R. Krishnan-Ayer, J. Photochem. Photobiol. C: Photochem. Rev. 9 (2008) 171–192.
[46] L. Pan, J.-J. Zou, X.-Y. Liu, X.-J. Liu, S. Wang, X. Zhang, L. Wang, Ind. Eng. Chem. Res. 51 (2012) 12782–12786.
[47] T. Hisatomi, J. Kubota, K. Domen, Chem. Soc. Rev. 43 (2014) 7520–7535.
[48] Z.-F. Huang, J. Song, L. Pan, X. Zhang, L. Wang, J.-J. Zou, Adv. Mater. 27 (2015) 5309–5327.
[49] S. Kment, Z. Hubicka, J. Krysa, D. Sekora, M. Zlamal, J. Olejnicek, M. Cada, P. Ksirova, Z. Remes, P. Schmuki, E. Schubert, R. Zboril, Appl. Catal. B: Environ. 165 (2015) 344–350.
[50] X. Chen, S.S. Mao, Chem. Rev. 107 (2007) 2891–2959.
[51] Z.-F. Huang, J. Song, L. Pan, X. Jia, Z. Li, J.-J. Zou, X. Zhang, L. Wang, Nanoscale 6 (2014) 8865–8872.
[52] S. Wang, L. Pan, J.-J. Song, W. Mi, J.-J. Zou, L. Wang, X. Zhang, J. Am. Chem. Soc. 137 (2015) 2975–2983.
[53] Z.-Y. Yuan, B.-L. Su, J. Mater. Chem. 16 (2006) 663–677.